JOURNAL OF MATERIALS SCIENCE 33 (1998) 2153–2163

Solid particle erosion resistance of ductile wrought superalloys and their weld overlay coatings

B. F. LEVIN, J. N. DUPONT, A. R. MARDER
Lehigh University, Energy Research Center, Bethlehem, PA 18015, USA
E-mail: bf12@lehigh.edu

The elevated temperature (400 °C) erosion behaviour of six weld overlay coatings and wrought alloys of similar compositions, was analysed and the relative ranking of their erosion resistance has been developed. Microhardness tests performed on eroded samples showed that all materials experienced significant plastic deformation. No relationship was observed between hardness of the coatings at 400 °C and their erosion resistance. A new toughness parameter was developed based on the measured area under the microhardness profile curve, which represents the ability of a material to absorb impact energy. This parameter correlated well with erosion resistance for both weld overlays and wrought alloys. Also, for the wrought alloys, an increase in area under the true stress–strain curve or tensile toughness, corresponded to an increase in erosion resistance. The physical significance of the toughness parameter is discussed along with relationships between hardness, tensile properties and erosion resistance. © *1998 Chapman & Hall*

1. Introduction

Solid particle erosion (SPE) is a loss of material during repetitive impacts of solid particles and is one of the primary reasons for the damage of power-generation components. Damage associated with SPE costs the utility industry at least $150 million annually in reduced efficiency of power generation [1]. One method to combat SPE is to select erosion resistant materials for use in components that are subject to an erosive environment. Therefore, the design and proper selection of erosion resistant materials can significantly reduce the operating cost of power-generation facilities.

Depending upon its mechanical properties, a material may erode by different mechanisms or a combination of mechanisms. Several researchers [2–4] established that the erosion mechanism for ductile materials shows certain common features, irrespective of the alloy type. In all cases, severe plastic deformation occurs in a localized region surrounding the point of particle impact. The description of material removal for ductile materials in terms of the mechanical properties was presented by Bitter [5]. During the impact, when the yield strength of the material is locally exceeded, plastic deformation takes place in the vicinity of the impact. After multiple impacts, a plastically deformed surface layer may form near the eroded surface, and therefore, the yield strength of the material increases due to strain hardening. Upon further deformation, the yield strength at the surface of the material will eventually become equal to its fracture strength and no further plastic deformation will occur. At this point, the material surface becomes brittle and its fragments may be removed by the subsequent impacts. Sundararajan and Shewmon [6] suggested that erosion of ductile materials can be accompanied by accommodation of the strain underneath the eroded surface. When a critical strain is exceeded in the deformation volume beneath the surface, material is detached from the eroded surface by ductile fracture.

Because the mechanical properties of a material are a reflection of its composition and microstructure, many attempts have been made to correlate erosion resistance to readily measurable mechanical properties. Some of these properties include hardness, ductility, yield strength, strain-hardening coefficient, and fatigue strength coefficient [7, 8]. For pure metals, some correlation between erosion rate and hardness has been shown [9]. However, several other observations have shown that the erosion rate is not dependent of material hardness [10–12]. Levy and Jahamir [12] demonstrated that an increase in the hardness of a plain carbon steel by microstructural modifications can lead to an increase in the erosion rate. Hutchings [13] emphasized that the effect of hardness on erosion resistance must be considered in relation to the erodent properties and erosion-test conditions.

In an attempt to correlate erosion resistance to various mechanical properties, several erosion models were developed [7]. Hutchings [14] proposed that cyclic fatigue is the dominant mechanism of material removal during erosion and derived an equation to predict erosion resistance. In this model, the erosion resistance is proportional to $H^{3/2}e_c^2$, where H is the dynamic hardness of a material and e_c is the critical strain to fracture. Other models were proposed to correlate erosion resistance to ductility [15], fatigue

strength [8], and yield strength [16]. Although these models showed a reasonable correlation with erosion resistance for different alloys, their major simplification is a neglect of the work hardening of ductile materials during particle impacts. However, because of work hardening, these materials exhibit a change in mechanical properties within the plastically deformed zone and therefore, modelling of the erosion behaviour becomes complex. The efforts to model erosion behaviour of ductile materials without considering the effect of work hardening do not accurately represent the mechanism of material removal.

Only a few attempts have been made to measure the plastic zone size that forms in ductile materials in the vicinity of the eroded surface [17–20]. It is particularly surprising, because the size of the plastically deformed region may represent a measure of energy absorbed before fracture during erosion. Only one erosion model [19] accounted for the plastic zone size. Assuming that the plastic zone depth is proportional to the size of the crater that forms during impact, the researchers concluded that erosion rate is proportional to L^3 (L is the plastic zone depth). However, this model contains several parameters that are not readily measurable, and therefore its applicability for selection of erosion resistant materials is limited. It was the purpose of this research to investigate the effect of mechanical properties on erosion resistance of various ductile alloys and coatings.

2. Experimental procedure

Six weld overlay coatings were selected for erosion testing. Their nominal chemical compositions are shown in Table I. Also, five wrought alloys with compositions similar to weld overlays (Ultimet, Inconel-625, Hastelloy-C22, 316L SS, and Stellite-6) were tested. A fully automatic welding laboratory was used for applying the weld alloys and the plasma transferred arc welding (PTAW) process was employed for coating deposition. All coatings were deposited on 1018 carbon steel substrates (30.5 cm × 30.5 cm × 0.64 cm thick). After deposition, the coatings were sectioned into 1.3 cm × 1.3 cm samples for erosion tests. The welding parameters such as voltage, travel speed, current, and filler metal feed rate were optimized in order to provide good fusion between the coating and substrate. Although coating thicknesses ranged from 1.8–4.3 mm, it did not affect relative erosion ranking of the welds because erosion resistance was determined based upon the volume loss of the coatings.

The erosion tester used in this study is described elsewhere [21]. The standard test conditions that were chosen for this study are seen in Table II. It should be noted that, because the erodent size was different for the wrought and weld alloys, a direct quantitative comparison between the erosion resistance of these materials cannot be made. The sample temperature was chosen to be 400 °C, similar to the temperature of a fireside boiler tube surface. Four or five different erosion exposure times were used in this study to adequately obtain the weight loss versus time plot for each material. One sample was used for each erosion time, and therefore, four or five samples from each material were used to obtain the weight loss versus erosion time plots, the slopes of which yield the steady-state erosion rate. To quantify weight loss during the erosion experiments, the erosion specimens were ultrasonically cleaned in acetone and weighed before and after the erosion tests to the nearest 0.1 mg. The volumetric erosion rates for each alloy were obtained by dividing weight loss rate by the density of the alloy.

In order to investigate the effect of hardness on erosion resistance at elevated temperature (400 °C), high-temperature microhardness tests were performed on a Nikon Microhardness Tester. The measurements were obtained on a transverse section of each weld overlay. Before testing, each sample was mechanically polished to a 0.3 μm surface finish. High-temperature hardness tests were made with a 500 g load using a Vickers indentor. Measurements were taken at 25 °C and 400 °C under 1 mPa (10^{-5} torr) pressure. Average microhardness numbers and standard deviations were calculated from at least ten indentations.

To determine the size of the deformed region beneath the eroded surface, microhardness tests were performed on a transverse section of each material after the longest exposure time (100 or 120 min) at

TABLE I Nominal chemical composition (wt %) of the selected alloys

Weld	Co	Ni	Fe	Cr	C	Other
Stellite-6	Bal.	3[a]	3	28–32	0.9–1.4	3.5–5.5W, 1.5Mo, 2Mn
Ultimet	Bal.	9	3	26	0.058	2W, 5Mo
Hastelloy-C22	–	Bal.	2–6	22–22.5	0.015	2.5–3.5W, 12.5–14.5Mo 0.35V
Inconel-625	–	Bal.	5	20–23	0.01	3.1–4.15 (Ta + Nb), 8–10Mo
Iron–aluminide	–	–	Bal.	2.1	0.023	14.8Al
316L SS	–	10–14	Bal.	16–18	0.03	2–3Mo, 1.5–2.5Mn

[a]All the single values are the maximum values.

TABLE II Erosion tests conditions

Eroded sample planar dimensions	1.27 cm × 1.27 cm
Sample temperature	400 °C
Erodent particle velocity	$40 \pm 5\ m\ s^{-1}$
Erodent particles flux	$8.56\ mg\ mm^{-2}\ s$
Impingement angle	90°
Erodent	Angular alumina (Al_2O_3)
Erodent size range	300–425 and 300–600 μm for wrought and weld alloys, respectively
Average diameter of the erodent	350 and 450 μm for wrought and weld alloys, respectively

a 90° particle impact angle. As a result of erosion, the material beneath the eroded surface may experience plastic deformation and the coating hardness may increase directly below the surface. A plastic zone size can be estimated by obtaining a microhardness profile from the eroded surface into the base material. In contrast to the hot hardness measurements for which the Vickers indentor was used, the plastic zone depth measurements were performed using a Knoop indentor with a test load of 10 g. The Knoop indentor minimizes the specimen edge effect on microhardness results, allowing the tests to begin at 10 μm from the eroded surface. The microhardness tests were conducted according to ASTM E 384 standard [22]. Three to five microhardness profiles were obtained in different locations of each material in order to improve the statistical significance of the data. From these profiles, the size of the plastic zone for each coating was estimated.

Tensile tests at 400 °C were performed for Ultimet, Inconel-625, C-22, 316L SS, and Stellite-6 wrought materials to investigate the effect of mechanical properties on erosion resistance at elevated temperature. The true stress–strain curves were obtained from the generated load–displacement data by using the conversion equations [23]. It should be noted that the mechanical properties of the wrought alloys and weld overlay coatings are different. However, the effect of mechanical properties on erosion resistance for the wrought materials should be similar to weld alloys and may yield information which is invaluable for selecting erosion resistant coatings and alloys based on their known mechanical properties. Tensile tests were performed according to the ASTM E-8 standard [24] at 400 °C in laboratory air. One small-size sample, 0.6 cm diameter and 2.4 cm gauge length, was tested for each material at the strain rate of $10^{-3}\,s^{-1}$.

The area under the true stress–strain diagram represents the amount of energy per unit volume a material can absorb before fracture. This parameter is also called tensile toughness. In order to determine the tensile toughness for each material, the area under the true stress–strain diagram was calculated. The tensile behaviour in the fully plastic region (up to fracture stress) can be approximated by the following power law expression [23]

$$\sigma = K\varepsilon^n \tag{1}$$

where K and n are the strength and strain-hardening coefficients of the material, respectively. Unfortunately, no simple single equation describes the entire stress–strain behaviour of the material. Therefore, in order to calculate the area under the stress–strain curve, the best-fit power law expression that describes plastic region and best-fit curve that describes the elastic and transition (elastic–plastic) region were found for each alloy. Then, these expressions were integrated to give the total area under the stress–strain curve or tensile toughness.

The as-welded and wrought samples were cross-sectioned and mounted in cold curing, thermosetting epoxy. Each sample was mechanically polished to a 0.3 μm surface finish and etched. All alloys are commercially available and their microstructures have been fully documented elsewhere [25–32]. Therefore, only light optical microscopy (LOM) analysis was performed in order to determine any differences in material microstructures. However, for the iron–aluminide weld overlay coating, electron probe microanalysis (EPMA) was performed to determine chemical composition across the weld. An EPMA trace was conducted across the entire overlay thickness from the fusion line area to the weld metal surface at accelerating voltage of 15 kV and beam current of ≈20 nA. Raw data were reduced to weight percentages using the ZAF algorithm [33].

3. Results and discussion

3.1. Microstructural characterization

Typical weld metal microstructures are presented in Fig. 1. The nickel base (Hastelloy C-22 and Inconel-625), cobalt base (Stellite-6 and Ultimet) and iron base (316L SS) overlays contain primary dendrites with interdendritic secondary phases. The interdendritic phases in Inconel-625 are typically NbC and/or Laves, depending mainly on the relative amounts of iron, niobium and carbon in the final overlay deposit [25–27]. In overlay application where the Inconel-625 weld metal composition is enriched in iron due to dilution from the substrate, Laves is the predominant second phase [26]. Stellite-6 typically forms M_7C_3 in the interdendritic regions at the terminal stages of solidification [28], whereas Hastelloy C-22 contains molybdenum-rich intermetallic σ, μ, and P phases [29]. The 316 stainless steel overlay contains a two-phase ferrite/austenite structure. The starting powder used for deposition of the iron aluminide exhibited the nominal Fe_3Al composition (Table I). However, microprobe data obtained on the as-deposited overlay revealed a reduced aluminium content of approximately 9 wt % due to dilution from the substrate. Reference to the Fe–Al binary diagram [30] suggests this composition is a solid solution of α-(Fe,Al). The iron–aluminide coating microstructure is significantly different from all the other coatings studied and the equiaxed grain morphology with fine precipitates can be seen from Fig. 1d. Little information is available in the open literature in microstructural evolution of welds in Ultimet [31].

Ultimet, Inconel-625, Hastelloy-C22, and 316L SS wrought alloys were annealed austenitic solid solutions and their microstructures were documented elsewhere [31, 32]. As an example, the microstructure of the wrought 316L SS with equiaxed grains is shown in Fig. 2. Microstructure of the wrought Stellite-6 alloy consists of hard carbide particles dispersed in austenitic matrix [32].

3.2. Erosion tests

A typical erosion weight loss versus time plots for Stellite-6 and Ultimet weld overlay coatings at 90° impact are shown in Fig. 3. For these coatings, erosion reached steady state after approximately 20 and 5 min exposure for Stellite-6 and Ultimet, respectively.

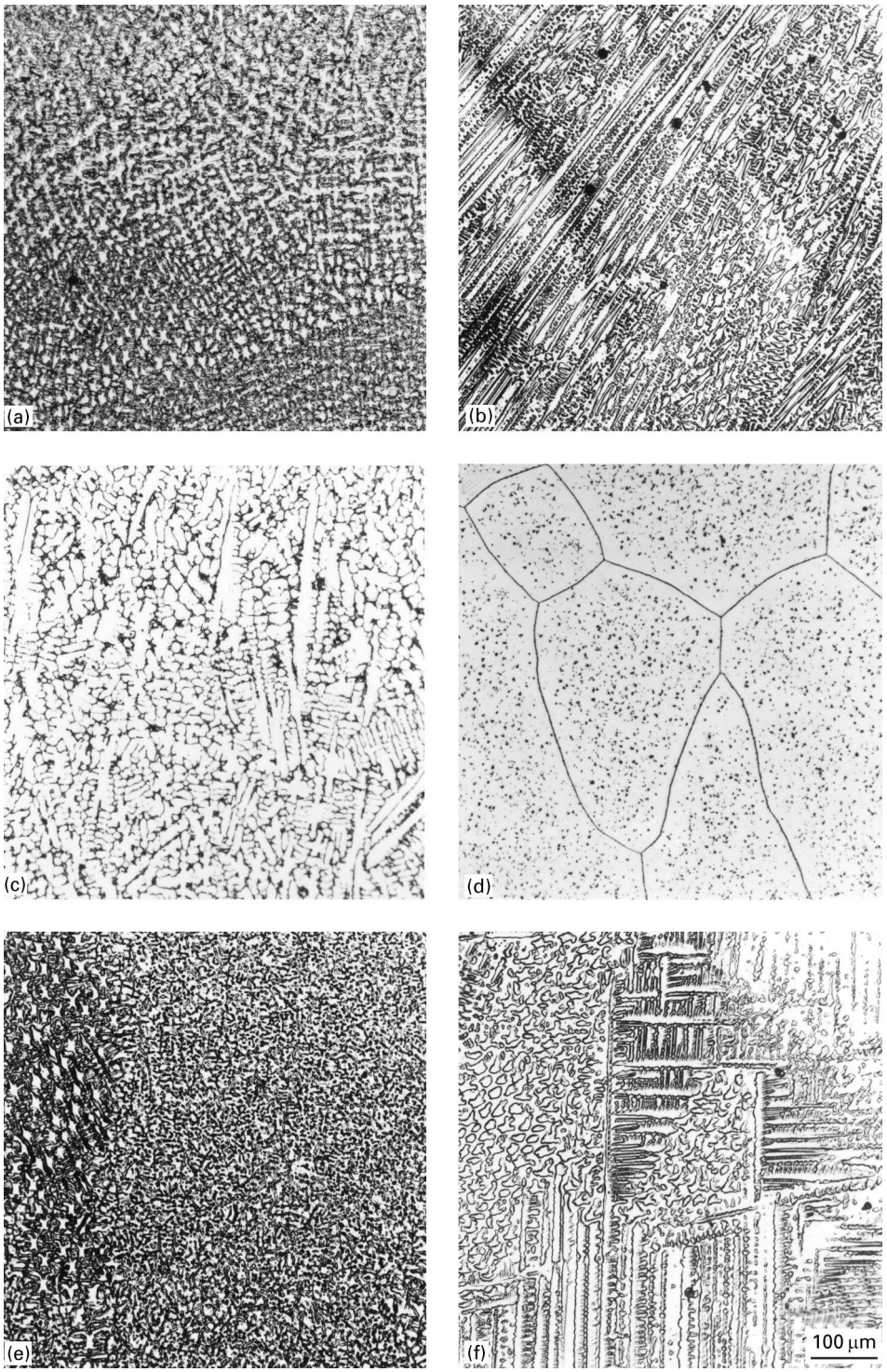

Figure 1 As-welded microstructure of the weld overlay coatings: (a) Inconel-625; (b) Hastelloy-C22; (c) Stellite-6, (d) Iron–Aluminide, (e) 316L SS, and (f) Ultimet.

The Stellite-6 coating showed a higher steady-state erosion rate (0.10 mg min^{-1}) than the Ultimet coating (0.072 mg min^{-1}). The relative ranking of weld overlay coatings and wrought alloys based upon their volumetric erosion rates at 400 °C are shown in Table III. The weld overlays such as Ultimet, Inconel-625, and 316L SS exhibited steady-state erosion rates that are lower than the erosion rates for the remaining coatings. Stellite-6 an alloy that is commercially used for abrasion protection, showed a relatively high erosion rate compared with Inconel-625 and 316L SS, coatings that are often selected for corrosion protection. Among the wrought alloys, Inconel-625 and Hastelloy-C22 offered the best erosion resistance, while Stellite-6 showed the worst erosion resistance.

3.3. Plastic deformation and erosion resistance

Microhardness tests were performed to measure the size of the deformed region beneath the eroded surface. It was found that, for both coatings and wrought alloys, microhardness significantly increases near the eroded surface (Figs 4 and 5, respectively). These

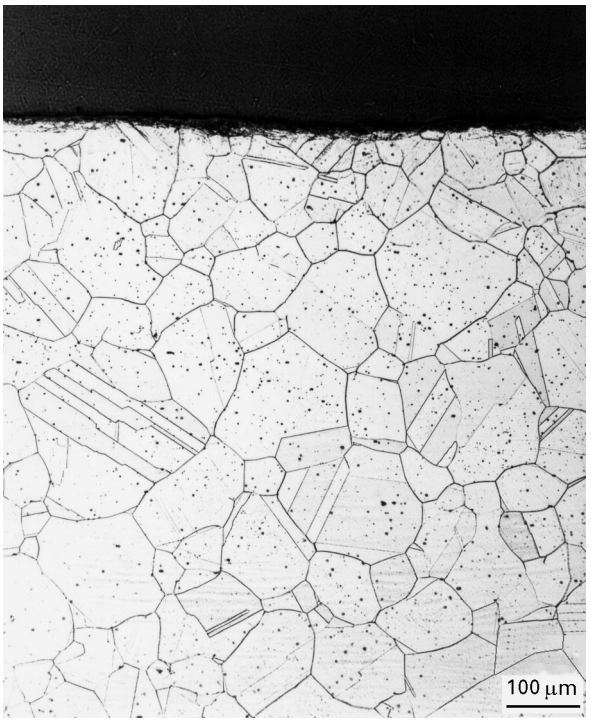

Figure 2 Microstructure of wrought 316L stainless steel showing equiaxed grains (etchant: 60% HNO_3–40% H_2O electrolytic solution at 4 V).

TABLE III Volumetric erosion rates for tested weld overlay coatings and wrought alloys at 400 °C and 90° impact angle

Weld overlay coatings/wrought alloys[a]	Erosion rate (10^3 mm^3 min^{-1})	
	Weld overlay	Wrought alloy
Ultimet	8.5 ± 0.3	3.6 ± 0.2
Inconel-625	9.4 ± 0.1	2.8 ± 0.1
316L SS	10.0 ± 0.4	6.9 ± 0.3
Iron–aluminide	11.0 ± 0.4	–
Hastelloy-22	11.4 ± 0.7	3.0 ± 0.1
Stellite-6	11.9 ± 0.4	8.9 ± 0.2

[a]Because the erodent size was different for the wrought and weld alloys, a direct quantitative comparison between the erosion resistance of weld overlays and wrought alloys cannot be made.

results show that, for all tested materials, a portion of the impacting particles kinetic energy is absorbed through plastic deformation with a subsequent increase in hardness at the eroded surface. To illustrate the importance of the material to absorb plastic deformation, a backscattered electron image of the eroded Stellite-6 wrought alloy is shown in Fig. 6. In this cross-section, it can be seen that the surface carbide (A) showed severe cracking due to the particle impacts. It can also be seen that a carbide located below the eroded surface (B) cracked due to the strain imposed by the plastically deformed layer. The carbides below the plastically deformed layer (20–25 μm) did not exhibit cracking. Although hardness determines the materials resistance to plastic deformation, no correlation was found between the volumetric erosion rates of weld overlay coatings at 400 °C and hardness at 400 °C (Fig. 7). Furthermore, the Stellite-6 weld overlay that exhibited the highest hardness also showed the highest erosion rate (0.0119 mm^3 min^{-1}) among weld overlays. Clearly, the ability of the ductile coatings to resist plastic deformation did not contribute to erosion resistance. Therefore, hardness is not the only material property that controls erosion resistance. These results show that, for all the studied materials, the erosion involves significant plastic deformation and, therefore, erosion resistance is controlled by the ability to absorb impact energy through plastic deformation.

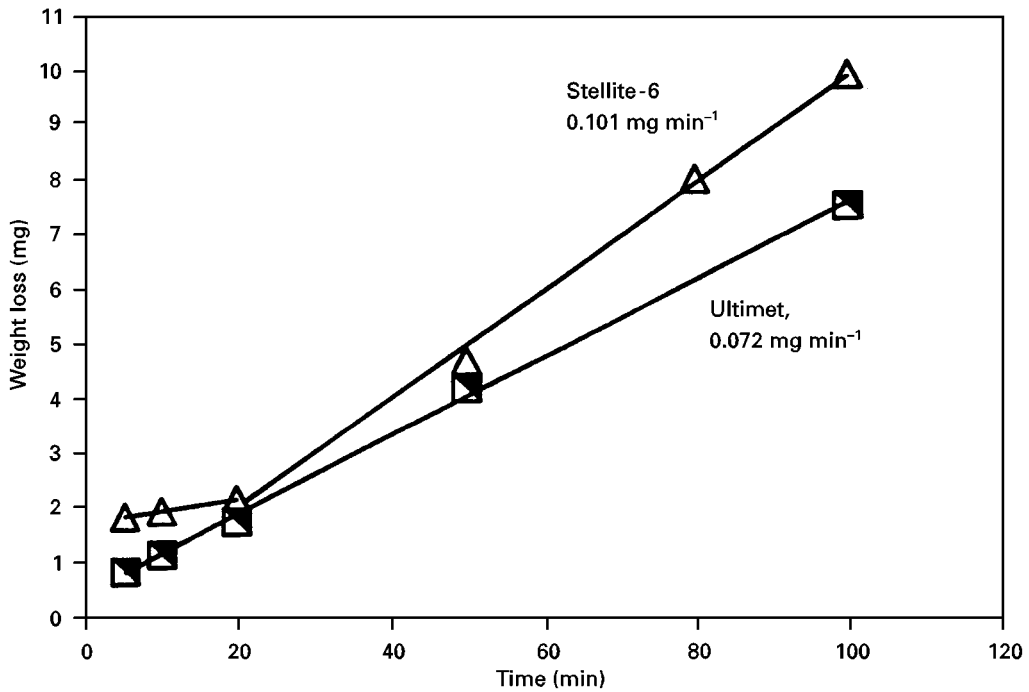

Figure 3 Weight loss as a function of time for Stellite-6 and Ultimet weld overlay coatings at 400 °C and 90° angle (Al_2O_3 erodent).

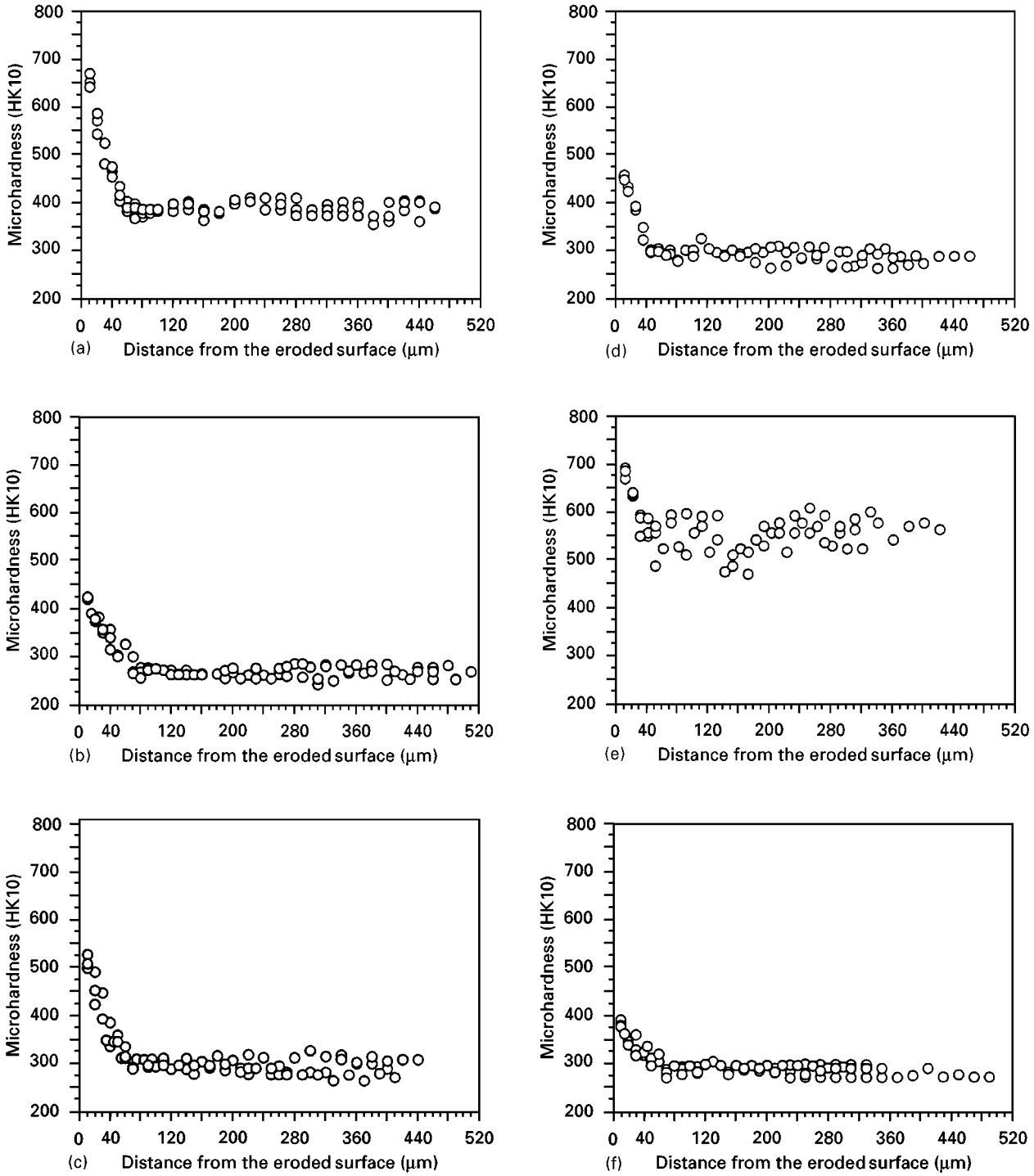

Figure 4 Microhardness profiles for weld overlay coatings after 100 min exposure in the erosion tester at 400 °C and 90° particle impact angle (Al_2O_3 erodent): (a) Ultimet, (b) 316L-SS, (c) Inconel-625, (d) Hastelloy-C22, (e) Stellite-6, (f) iron–aluminide.

3.3.1. Mechanism of energy dissipation during erosion at normal impact angle

The relative ability of overlays and wrought alloys to dissipate particle impact energy can be determined by calculating the area under the curve of microhardness versus distance from the eroded surface. This area can be interpreted as a measure of the amount of energy that the material absorbs during particle impact before it reaches the critical fracture stress. The analogy between the true stress–strain curve and the microhardness profile curve after erosion may be appropriate. The area under the stress–strain curve represents the energy per unit volume that the material can absorb before fracture. For the microhardness profiles, the hardness of the material can be correlated to its strength within a reasonable approximation. This relationship can be in the form of $H = A\sigma_y$, where H is the hardness, σ_y is the yield strength, and A is a constant [34]. A schematic illustration of the change in microhardness with depth below the eroded surface is shown in Fig. 8. The microhardness profile curve represents the variation in strength beneath the eroded surface with strain imposed by particle impacts. The decrease in hardness with distance from the eroded surface is caused by a decrease in strain.

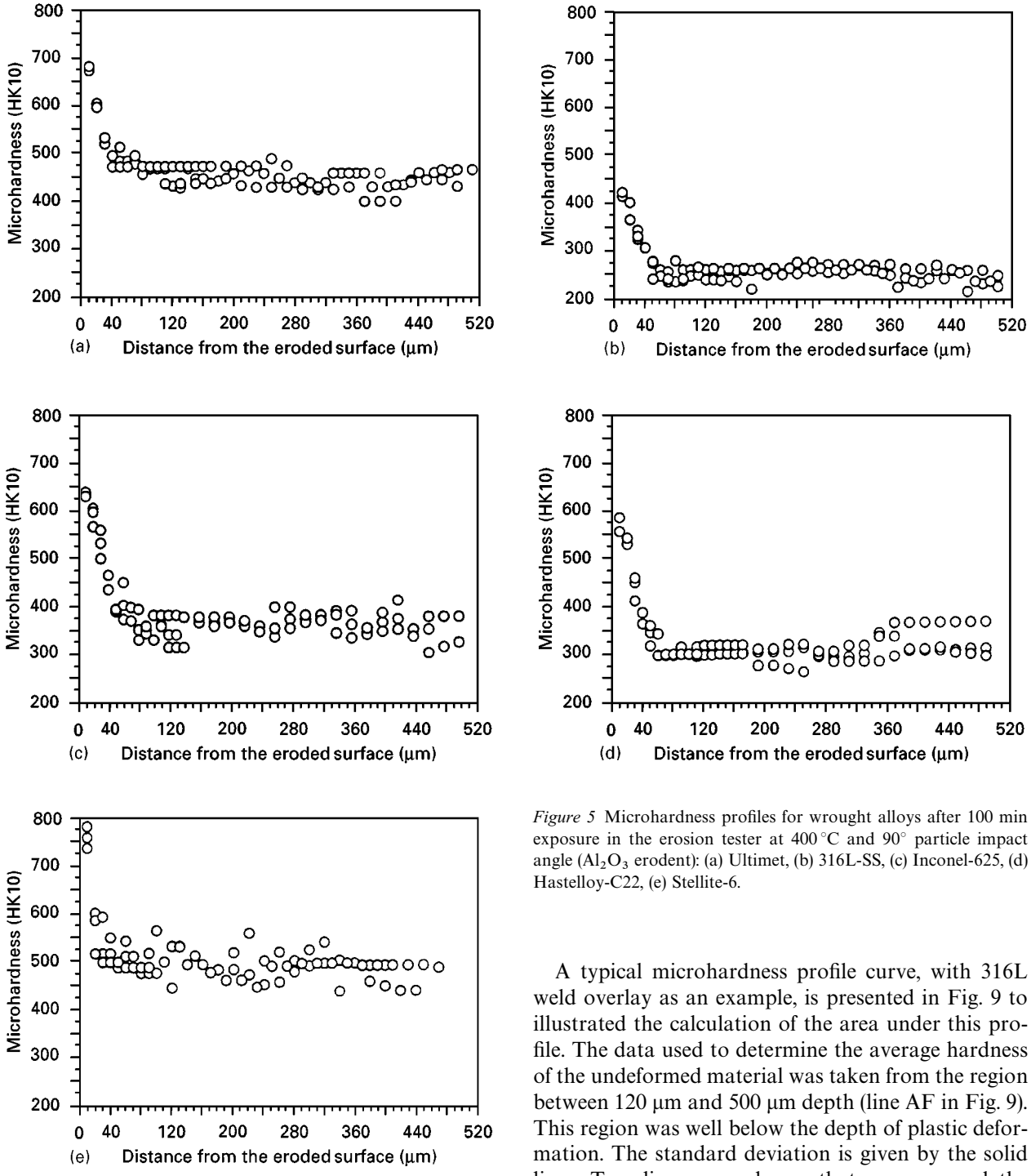

Figure 5 Microhardness profiles for wrought alloys after 100 min exposure in the erosion tester at 400 °C and 90° particle impact angle (Al_2O_3 erodent): (a) Ultimet, (b) 316L-SS, (c) Inconel-625, (d) Hastelloy-C22, (e) Stellite-6.

Therefore, hardness versus distance from the eroded surface curve can be qualitatively correlated to the stress–strain curve (see Fig. 8). By analogy with the true stress–strain curve, the area under the hardness–distance curve may be interpreted as a measure of energy that a material can absorb during erosion before it will experience localized fracture and weight loss at the surface. It should be noted that the analogy between the true stress–strain diagram and the microhardness profile is only qualitative because the conventional stress–strain diagram is obtained by loading at low strain rates while microhardness profiles were obtained after particle impacts that impose high strain rates.

A typical microhardness profile curve, with 316L weld overlay as an example, is presented in Fig. 9 to illustrated the calculation of the area under this profile. The data used to determine the average hardness of the undeformed material was taken from the region between 120 μm and 500 μm depth (line AF in Fig. 9). This region was well below the depth of plastic deformation. The standard deviation is given by the solid lines. Two lines were drawn that encompassed the data in the plastic zone region given by BD and CE in Fig. 9. These lines envelope the hardness data within the plastic zone. The minimum and maximum areas under the curve were found by calculating areas ABD and ACE, respectively ($\text{Area}_{ABD} = 0.5 \times AB \times AD$ and $\text{Area}_{ACE} = 0.5 \times AC \times AE$). From these data, an average area under the curve was calculated.

3.3.2. Area under the microhardness curve and erosion resistance

The volumetric erosion rates for coatings and wrought alloys are plotted versus the average area under the microhardness profile curves in Fig. 10a and b, respectively. It can be seen that, as the area under the curve increases, the volumetric erosion rate decreases. The "area under the curve" parameter includes the

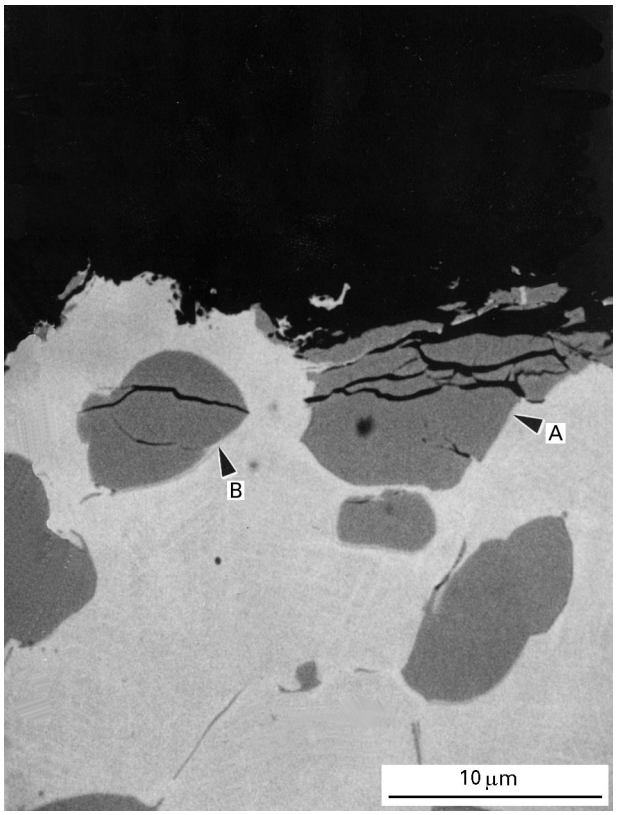

Figure 6 Backscattered electron image of the cross-section of eroded Stellite-6 wrought alloy (400 °C, 90° impact angle, Al_2O_3 erodent).

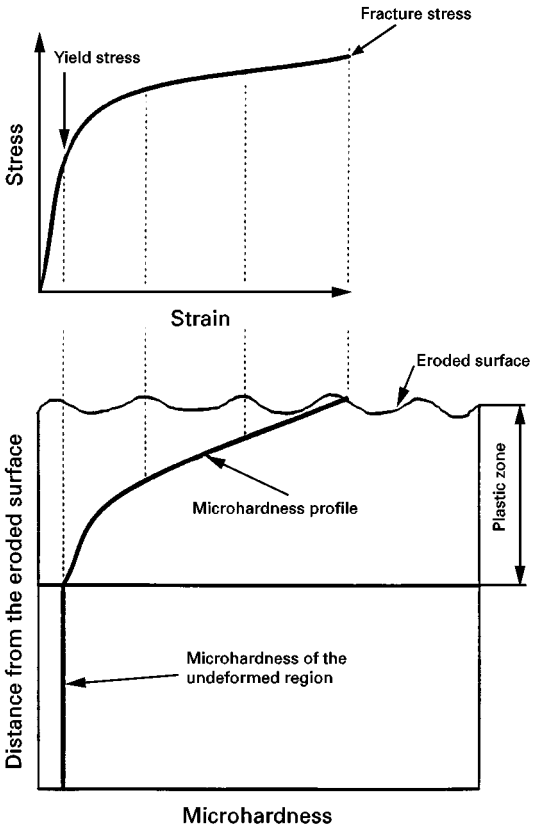

Figure 8 A schematic diagram of change in microhardness with distance from the eroded surface. Correlation between the true stress–strain diagram and microhardness profile is only qualitative.

increase in surface hardness ($H_{surface} - H_{bulk}$) due to particle impacts and the distance over which this increase occurred (plastic zone size). An increase in surface hardness due to erosion represents the material's ability to strain harden, while the plastic zone size shows the depth over which strain hardening occurs. For example, materials with a high ability to strain harden – high ($H_{surface} - H_{bulk}$) – require a higher applied stress to exceed the critical fracture strength than materials with a low ability to strain harden – small ($H_{surface} - H_{bulk}$). However, if this increase in strength (due to strain hardening) occurs over a small volume, fracture will occur fairly easily because deformation is localized and fracture strength can be reach-

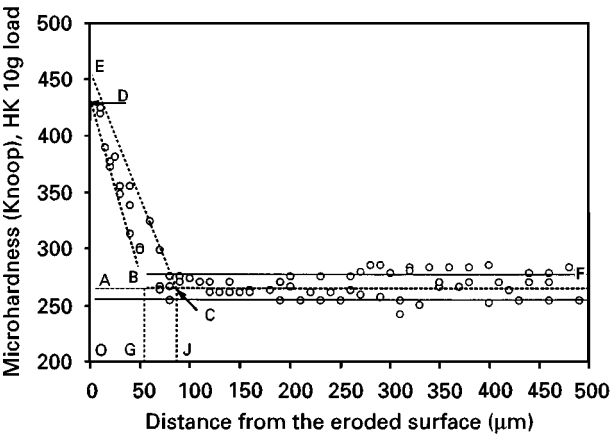

Figure 9 A typical example of the microhardness profile (316L SS Coating) from which the area under the curve can be determined. AF, average base hardness; OG, minimum plastic zone; OJ, maximum plastic zone; ABD, minimum area under the curve; ACE, maximum area under the curve; AD, minimum ΔHK; AE, maximum ΔHK.

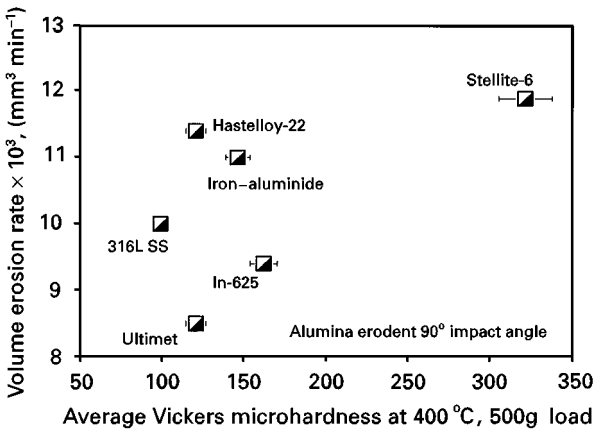

Figure 7 Effect of hardness at 400 °C on volume erosion rates at 400 °C for plastically deformed weld overlay coatings (90° impact angle, Al_2O_3 erodent).

ed after relatively few impacts. On the other hand, if the material has a large plastic zone size but has low ability to strain harden – low ($H_{surface} - H_{bulk}$) – it will also fracture after relatively few impacts. In this case, fracture may occur because only a small applied stress is needed to exceed the fracture strength of the material. To illustrate that a large plastic zone size is not a sufficient requirement for erosion resistance, the volume erosion rates are plotted versus plastic zone size in Fig. 11. No correlation can be seen between these two parameters. These measurements showed

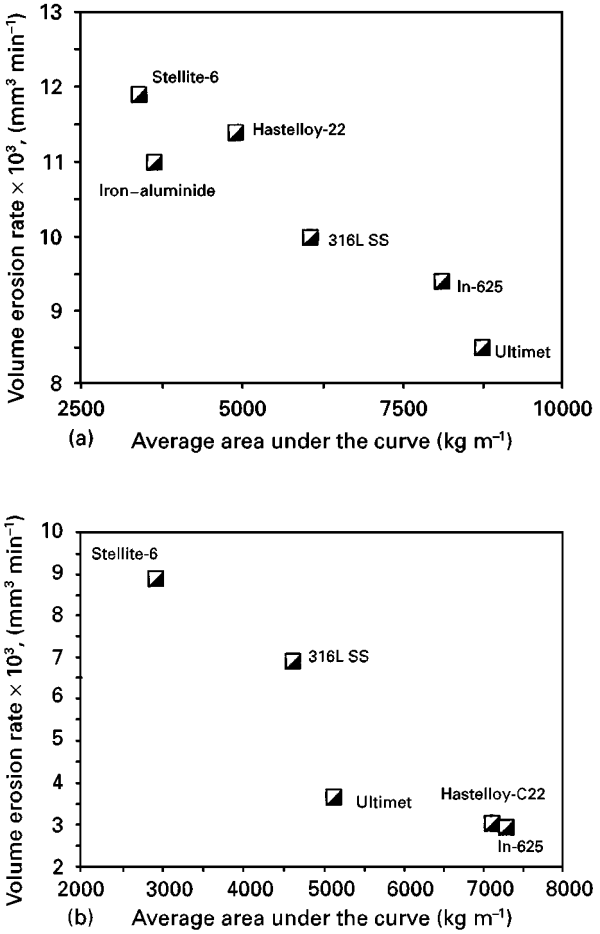

Figure 10 Effect of calculated area under the curve of microhardness versus distance from the eroded surface on volume erosion rates for (a) weld overlay coatings and (b) wrought alloys (90° impact angle, Al_2O_3 erodent).

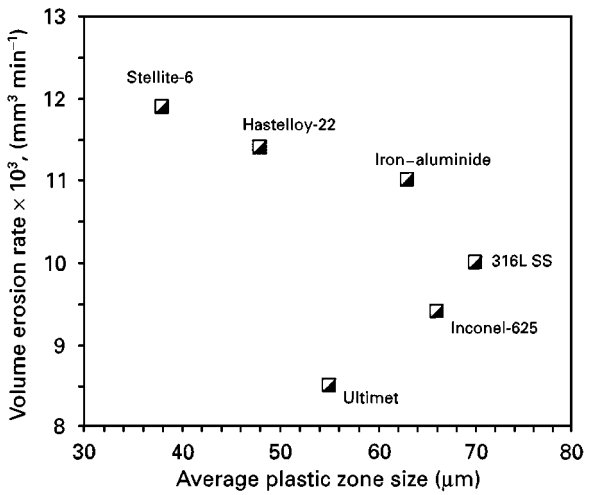

Figure 11 Effect of the measured plastic zone size on volume erosion rates for weld overlay coatings (90° impact angle, Al_2O_3 erodent).

that a large plastic zone size does not necessarily lead to a high erosion resistance. The calculated area under the curve is a better representation of erosion resistance because it includes both strain hardening and plastic zone depth. If the energy to fracture increases ("area under the curve" increases), erosion resistance also increases.

It is important to note that the effect of "area under the microhardness curve" was similar for weld overlays and wrought alloys, suggesting that this parameter may be used to explain erosion behaviour of various ductile alloy systems. Although the "area under the microhardness curve" showed good correlation with erosion resistance, it is not easily measurable and requires post-erosion analysis of the material. Therefore, it is essential to find a mechanical property or combination of properties that correlate to the "area under the microhardness curve" and represent the energy that a material absorbs during erosion. By accomplishing this task, erosion resistant materials can be selected based upon mechanical properties.

3.3.3. Tensile toughness and erosion resistance

Considering the similarities between true stress–strain curves and microhardness profile curves, tensile toughness may contribute to the erosion resistance of ductile materials. The tensile toughness values for wrought alloys at 400 °C were determined by integrating the area under true stress–strain curves that are presented in Fig. 12. The effect of tensile toughness on the erosion resistance of wrought alloys is shown in Fig. 13. It can be seen that alloys with the lowest tensile toughness (Stellite-6) showed the lowest

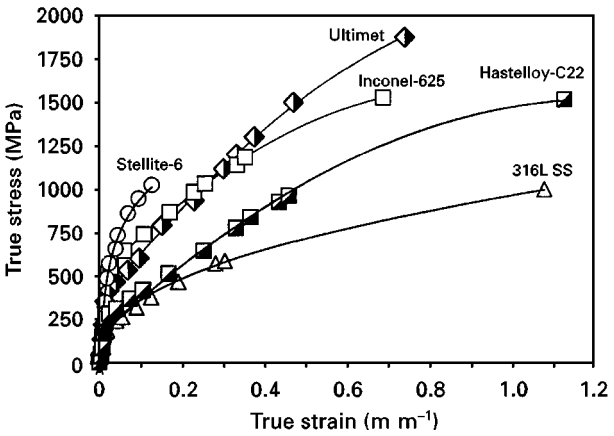

Figure 12 True stress–strain curves for wrought alloys at 400 °C.

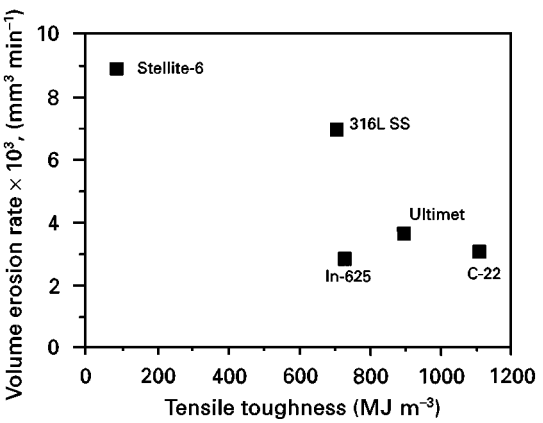

Figure 13 Effect of tensile toughness at 400 °C on volume erosion rates at 400 °C for wrought alloys (90° impact angle, Al_2O_3 erodent).

erosion resistance while materials with much higher tensile toughness (Ultimet, Inconel-625, and C-22) showed much higher erosion resistance. The equation for the tensile toughness of the material can be found by integrating the stress–strain function (Equation 1) from zero to failure strain. Therefore, tensile toughness can be described as

$$T = K\left(\frac{\varepsilon_f^{n+1}}{n+1}\right) \tag{2}$$

where T is the tensile toughness, n is the strain-hardening coefficient and ε_f is the failure strain. This equation shows that the toughness of a material represents the combined effect of strength, strain-hardening coefficient, and ductility on energy absorption during the deformation process. Therefore, toughness is a better indicator of the behaviour of a material during erosion than any single property that contributes to toughness.

Although a trend of an increase in erosion resistance with an increase in tensile toughness was observed, the Inconel-625 alloy, that had a lower toughness than Ultimet and C-22 alloys, showed better erosion resistance than these alloys. To consider the validity of the qualitative analogy between true stress–strain curve and microhardness profile curve, the area under the stress–strain diagram is plotted against the area under the microhardness curve in Fig. 14. It can be seen that a reasonable correlation exists between these two parameters. However, Inconel-625 alloy deviated from this correlation possibly because of a strain-rate effect. Hutchings [35] calculated that strain rates during erosion range between 10^3 and $10^7\ s^{-1}$, while strain rates during quasi-static tensile or compression tests vary between 10^{-4} and $10^{-1}\ s^{-1}$. Therefore, if the tested materials are strain-rate sensitive the toughness measured from tensile tests might be different from the toughness during solid particle erosion. Therefore, at high strain rates, Inconel-625 may have a higher toughness than the other tested alloys. In addition, Inconel-625 alloy has a higher yield strength than Ultimet and C-22 alloy (630, 450, and 320 MPa, respectively). Therefore, a higher applied stress is needed to cause plastic deformation for this alloy. Thus a combination of (1) high yield strength, to prevent plastic deformation, and (2) tensile toughness, to absorb plastic deformation, is responsible for the excellent erosion resistance.

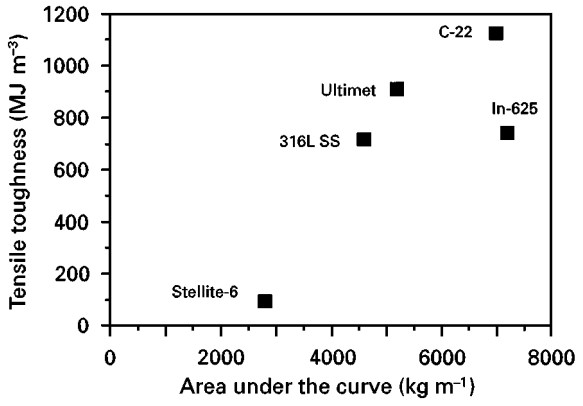

Figure 14 Effect of tensile toughness at 400 °C on the calculated area under the microhardness curve after erosion at 400 °C for wrought alloys (90° impact angle, Al_2O_3 erodent).

4. Conclusions

1. The relative ranking of erosion resistance of weld overlay coatings and wrought alloys at 400 °C has been developed. The Ultimet, Inconel-625, and 316L SS coatings showed considerably lower erosion rates than the remaining coatings. Among the wrought alloys, the Inconel-625 and Hastelloy-C22 alloys exhibited the lowest erosion rates.

2. A new toughness parameter, "area under the microhardness curve", that represents the ability of a material to absorb impact energy, was developed and correlated well with erosion resistance.

3. For both coatings and wrought alloys, an increase in the area under the microhardness profile curve led to an increase in their erosion resistance. Ductile materials that are able to strain harden – high ($H_{surface} - H_{bulk}$) – over large distances (large plastic zone) may have a higher energy to fracture and, therefore, good erosion resistance. For the wrought alloys, an increase in area under the true stress–strain curve or tensile toughness corresponded to an increase in erosion resistance.

Acknowledgements

This work was made possible by financial support from the US Department of Energy Under Grant DE-FG22-92PS92542 and Air Products and Chemicals Inc. The authors also thank Mr A. O. Benscoter, Dr B. Lindsley and Dr B. J. Smith for their help in sample preparation and helpful discussions.

References

1 L. LAMMARRE, *J. EPRI*, October/November (1990) 31.
2. I. M. HUTCHINGS, R. E. WINTER and J. E. FIELD, *Proc. R. Soc. Lond. Ser. A* **348** (1976) 379.
3. I. M. HUTCHINGS and A. V. LEVY, *Wear* **131** (1981) 105.
4. P. VEERABHADRA RAO, S. G. YOUNG and D. H. BUCKLEY, *ibid.* **85** (1983) 223.
5. J. G. A. BITTER, *ibid.* **6** (1963) 5.
6. G. SUNDARARAJAN and P. G. SHEWMON, *ibid.* **84** (1983) 237.
7. H. C. MENG and K. C. LUDEMA, *ibid.* **181–183** (1995) 443.
8. R. H. RICHMAN and W. P. McNAUGHTON, *ibid.* **140** (1990) 63.
9. I. FINNIE, J. WOLAK and Y. KABIL, *J. Mater.* **2** (1967) 682.
10. A. V. LEVY, "Solid Particle Erosion and Erosion-Corrosion of Metals" (ASM International, Materials Park, OH, 1995) p. 43.
11. B. F. LEVIN, J. N. DUPONT and A. R. MARDER, *Wear* **181–183** (1995) 810.
12. A. LEVY and D. JAHAMIR, in "Corrosion-Erosion Behaviour Of Materials", edited by K. Natesan (Metallurgical Society of AIME, New York, 1980) p. 177.
13. I. M. HUTCHINGS, *J. Appl. Phys.* **25** (1986) A212.
14. *Idem.*, *Wear* **70** (1981) 269.
15. T. FOLEY and A. V. LEVY, *ibid.* **91**(1) (1983) 45.

16. I. FINNIE, *ibid.* **3** (1960) 87.
17. S. SODERBERG, S. HOGMARK and H. SWAHN, *ASLE Trans.* **26**(2) (1982) 161.
18. A. V. REDDY, G. SUNDARARAJAN, R. SIVAKUMAR and P. RAMA RAO, *Acta Metall.* **32** (1984) 1305.
19. A. V. REDDY and G. SUNDARARAJAN, *Wear* **111** (1986) 313.
20. M. RAO and J. R. KEISER, *Report. ORNL/TM*-11946, Prepared for the US Department of Energy, Oak Ridge National Laboratory, Oak Ridge, TN, March 1992.
21. B. LINDSLEY, K. STEIN and A. R. MARDER, *Meas. Sci. Technol.* **6** (1995) 1169.
22. ASTM E 384 Standard, Annual Book of ASTM Standards, Vol. 03.01, "Metals Tests Methods and Analytical Procedures" (American Society for Testing and Materials, Philadelphia, PA, 1988).
23. W. F. HOSFORD and R. M. CADELL, "Metal Forming Mechanics and Metallurgy", (Prentice-Hall, Englewood Cliffs, NJ, 1983) p. 80.
24. ASTM E 8 Standard, Annual Book of ASTM Standards, Vol. 03.01, "Metals Tests Methods and Analytical Procedures" (American Society for Testing and Materials, Philadelphia, PA, 1988).
25. M. J. CIESLAK, T. J. HEADLEY, T. J. KOLLIE and A. D. ROMIG Jr, *Metall. Trans.* **19A** (1988) 2319.
26. J. N. DUPONT, *Metall. Trans* **27A** (1996) 3612–3620
27. Q. H. ZHAO, Y. P. GAO, J. H. DEVLETIAN, J. M. McCARTHY and W. E. WOOD, in "International Trends in Welding Science and Technology", Proceedings of the 3rd International Conference, S. A. David and J. M. Vitek (ASM, Materials Park, OH, 1992) p. 339.
28. W. L. SILENCE, *Wear Mater.* Vol. **I** (1985) 77.
29. M. J. CIESLAK, T. J. HEADLEY and A. D. ROMIG Jr, *Metall. Trans* **17A** (1986) 2035.
30. "Alloy Phase Diagrams", ASM Handbook, Vol. 3 (American Society for Metals, Materials Park, OH, 1992) p. 2044.
31. S. J. MATHEWS, P. CROOK, L. H. FLASCHE and J. W. TACKET, *Weld. J.* **70** (1991) 331s.
32. "Metallography and Microstructures", ASM Handbook, 9th Edn, Vol. 9 (American Society for Metals, Materials Park, OH, 1985) p. 279.
33. K. F. J. HEINRICH, in "Microbeam Analysis", Proceedings of the 21st International Conference, edited by A. D. Romig Jr and W. F. Chambers (Albuquerque, New Mexico, 1986) p. 279.
34. D. TABOR, "The Hardness of Metals" (Clarendon Press, Oxford, 1951).
35. I. M. HUTCHINGS, *J. Phys. D Appl. Phys.* **10** (1977) L179.

Received 22 November 1996
and accepted 5 December 1997